



This is a repository copy of *Heterojunction-redox catalysts of FexCoyMg10CaO for high-temperature CO2 capture and in situ conversion in the context of green manufacturing.*

White Rose Research Online URL for this paper:
<https://eprints.whiterose.ac.uk/171222/>

Version: Accepted Version

Article:

Shao, B., Hu, G., Alkebsi, K.A.M. et al. (7 more authors) (2021) Heterojunction-redox catalysts of FexCoyMg10CaO for high-temperature CO2 capture and in situ conversion in the context of green manufacturing. *Energy & Environmental Science*, 14 (4). pp. 2291-2301. ISSN 1754-5692

<https://doi.org/10.1039/d0ee03320k>

© 2020 The Royal Society of Chemistry. This is an author-produced version of a paper subsequently published in *Energy & Environmental Science*. Uploaded in accordance with the publisher's self-archiving policy.

Reuse

Items deposited in White Rose Research Online are protected by copyright, with all rights reserved unless indicated otherwise. They may be downloaded and/or printed for private study, or other acts as permitted by national copyright laws. The publisher or other rights holders may allow further reproduction and re-use of the full text version. This is indicated by the licence information on the White Rose Research Online record for the item.

Takedown

If you consider content in White Rose Research Online to be in breach of UK law, please notify us by emailing eprints@whiterose.ac.uk including the URL of the record and the reason for the withdrawal request.



eprints@whiterose.ac.uk
<https://eprints.whiterose.ac.uk/>

Heterojunction-Redox Catalysts of $\text{Fe}_x\text{Co}_y\text{Mg}_{10}\text{CaO}$ for High-Temperature CO_2 Capture and In-situ Conversion in the Context of Green Manufacturing

Received 00th January 20xx,
Accepted 00th January 20xx

DOI: 10.1039/x0xx00000x

Bin Shao^a, Guihua Hu^b, Khalil A. M. Alkebsi^b, Guanghua Ye^c, Xiaoqing Lin^a, Wenli Du^b, Jun Hu^{a*}, Meihong Wang^{d*}, Honglai Liu^a and Feng Qian^b

The integration of carbon capture and CO_2 utilization could be a promising solution to the crisis of global warming. By integrating the calcium-looping (CaL) and the reverse-water-gas-shift (RWGS) reaction, a high-temperature CO_2 capture and in-situ conversion technology is successfully realized in one fixed-bed column at the same operating temperature of 650°C . Inspired by the heterojunction photocatalytic mechanism, the heterojunction-redox catalysis strategy is proposed for the first time by doping bimetallic $\text{Fe}^{3+}/\text{Fe}^{2+}$ and $\text{Co}^{3+}/\text{Co}^{2+}$ redox couples into a hierarchical porous CaO/MgO composite. The presence of different valence states of doped Fe and Co oxides not only provides extra oxygen vacancies to facilitate CO_2 adsorption, and hence the adsorption enhanced conversion (AEC); but also significantly lowers the electric potential difference of $\text{Fe}^{3+}/\text{Fe}^{2+}$ through the newly formed Fermi level in $\text{Fe}_5\text{Co}_5\text{Mg}_{10}\text{CaO}$, which makes the electron spillover easier to improve the catalytic activity in the RWGS reaction for CO_2 conversion. More importantly, with the high-temperature refractory of MgO and the highly dispersed Fe and Co oxides in $\text{Fe}_5\text{Co}_5\text{Mg}_{10}\text{CaO}$, the problem of CaO sintering is successfully solved. An excellent and stable high-temperature CO_2 capture capacity of $9.0\text{--}9.2\text{ mmol g}^{-1}$, an in-situ CO_2 conversion efficiency nearly 90 % and a CO selectivity close to 100 % are achieved in the integrated CaL/RWGS process. In addition, the experimental and simulation scale-up studies further demonstrate its practical scalability. Economic evaluation reveals that the integrated CaL/RWGS technology is much more cost-effective than the separated CaL and RWGS processes. Therefore, the heterojunction-redox strategy provides a unique way to design bifunctional adsorbent/catalyst materials. The integrated CaL/RWGS process could be a promising technology for CO_2 capture and utilization.

Introduction

With the increasing crisis of global warming, carbon capture, utilization and storage (CCUS) technology has been demonstrated to be an effective solution to address the global climate change.^{1–4} Currently, most CCUS studies focus on the power generation sector and explore carbon capture, utilization and storage separately. Accordingly, after carbon capture, CO_2 purification, compression and transportation are necessary for further sequestration, which consume a huge amount of energy.^{5–7} Moreover, the CO_2 emission from industry accounting for about 25% of total global CO_2 emission⁸ has not been systematically explored. It is worth mentioning the temperature of flue gas from the furnaces of industrial process is usually very high. For example, the flue gas temperature from thermal cracking furnace in the ethylene

industry is as high as $1,000^\circ\text{C}$. It is reported that the global production capacity of ethylene is around 170 million tons per year. Manufacturing one ton of ethylene produces between 1 to 2 tons of CO_2 .⁹ A huge amount of energy is needed for cooling so that the low-temperature CO_2 capture ($50\text{--}60^\circ\text{C}$) can be applied, and even more energy is consumed for heating again to realize the high-temperature CO_2 conversion ($>300^\circ\text{C}$).^{10, 11} Therefore, developing an integrated process combining carbon capture and utilization could be a promising solution in the context of green manufacturing.^{12, 13} If this integrated process can be operated in the same column under the same high temperature, it can significantly reduce the capital and operating cost, and also the energy consumption.^{14, 15}

A few pioneering studies have been performed to integrate carbon capture and carbon conversion. Farrauto's group fabricated a Ru/CaO composite to capture CO_2 and subsequently to produce CH_4 at the same temperature of 320°C in the same column.^{16, 17} Urakawa's group synthesized $\text{Ni-K}/\text{ZrO}_2$ and showed a synergistic effect on CO_2 methanation reaction.¹⁸ González-Velasco's group synthesized $\text{Ni-CaO}/\text{Al}_2\text{O}_3$ and $\text{Ni-Na}_2\text{CO}_3/\text{Al}_2\text{O}_3$ with Ni as the catalytic active site to integrate CO_2 capture and methanation conversion.¹⁹ However, the low CO_2 capture capacity seriously impeded the development of this integration strategy. **There remain** great challenges to develop dual function materials (DFMs) with

^aSchool of Chemistry and Molecular Engineering, East China University of Science and Technology, 130 Meilong Road, Shanghai 200237, China.

^bKey Laboratory of Advanced Control and Optimization for Chemical Processes of Ministry of Education, East China University of Science and Technology, 130 Meilong Road, Shanghai 200237, China

^cState Key Laboratory of Chemical Engineering, East China University of Science and Technology, 130 Meilong Road, Shanghai 200237, China.

^dDepartment of Chemical and Biological Engineering, The University of Sheffield, Sheffield S1 3JD, United Kingdom.

*Electronic Supplementary Information (ESI) available: [details of any supplementary information available should be included here]. See DOI: 10.1039/x0xx00000x

both excellent CO₂ capture capacity and high-efficient catalytic activity to convert the adsorbed CO₂ into high value-added chemicals.²⁰ Another challenge comes from the temperature matching between CO₂ capture and conversion. Most CO₂ conversion reactions take place at a high temperature, but conventional adsorbents prefer a low temperature and **do not** maintain the stability at such a high temperature.

Among various CO₂ capture technologies, the calcium-looping (CaL) process based on the reversible carbonation/calcination reactions at high temperature has attracted significant attention. The techno-economic evaluation of CaL revealed that its carbon capture cost is competitive to the current amine scrubbing technology²¹ because of the high reactivity with CO₂ (theoretical capture capacity of CaO is 17.8 mmol g⁻¹)²² and the abundantly available and low-price natural CaO source.²³ **However, CaO is easily sintered due to the pore collapse and agglomeration during** carbonation-calcination cycles at high temperature, leading to a rapid decrease of its surface area and thus its reactivity loss towards CO₂ due to the relatively low Tammann temperature of CaCO₃ (533 °C).²⁴ Many efforts have been devoted to solving this sintering problem.²⁵ Among them, one promising strategy is to use inert additives such as high-temperature refractory oxides of Al₂O₃,^{26, 27} ZrO₂,²⁸ TiO₂,²⁹ SiO₂,³⁰ MgO³¹ and the inert metals of K³², Sr³³ and Ga³⁴ to effectively improve the thermal stability of CaO. An alternative strategy is to construct porosity in CaO to prevent sintering. In previous work, we had successfully applied mesoporous CaO in a stable high-temperature CO₂ capture.³⁵ **The** porous CaO can not only enhance the CO₂ capture performance, but also act as a good substrate for loading metal catalysts. Very recently, the group led by Wu and Huang prepared a porous Ca₁Ni_{0.1}Ce_{0.033} by a sol-gel method, which exhibited high adsorption capacity and catalytic stability.³⁶ However, the CO₂ conversion efficiency by the reverse-water-gas-shift (RWGS) reaction is still not high enough, compromising the overall performance.

The RWGS reaction is one of the established reactions for CO₂ conversion³⁷⁻³⁹ and the produced CO can be an industrial feedstock for further conversion to valuable chemicals and fuels through well-developed syngas conversion technologies, such as Fischer-Tropsch synthesis^{40, 41} and Monsanto/Cativa acetic acid synthesis.^{42, 43} Various heterogeneous transition metal-based catalysts such as Cu, Pd, Au, Pt, Ni, Re, Rh, Ru, Co, Fe and Mo supported over metal oxides of MgO, TiO₂, SiO₂ or Al₂O₃ have been explored within the temperature range of 200-600 °C.⁴⁴⁻⁴⁶ As the RWGS reaction is slightly endothermic, a higher temperature is more favourable.³⁷ This provides a possibility to match the high temperature of CaL CO₂ capture.

In this study, we investigate carbon capture and in-situ CO₂ conversion by integrating CaL and RWGS reaction in the same column and operating at the same temperature. Through a simple one-pot sol-gel method, bimetallic Fe/Co catalysts and a high-temperature refractory MgO were doped into porous CaO. The structures of the obtained **Fe_xCo_yMg₁₀CaO** were well characterized to reveal their contributions to the simultaneous CO₂ capture capacity and catalytic conversion efficiency. Among them, **Fe₅Co₅Mg₁₀CaO** exhibited the best

performance for simultaneous CO₂ capture and conversion, superior to the reported works so far to our best knowledge. A heterojunction-redox mechanism of bimetallic catalysts was proposed for the first time to illustrate this superior catalytic performance. In addition, we evaluated the scale-up potential and economic benefits of this integrated CaL/RWGS technology. Therefore, a novel strategy for simultaneous CO₂ capture and utilization has been developed in this study.

Experimental

Synthesis

Fe_xCo_yMg₁₀CaO was prepared through a simple one-pot sol-gel method⁴⁷ and subsequent calcination. Typically, 8.43 g of calcium nitrate tetrahydrate (equivalent to 2 g CaO) and 2.133 g magnesium nitrate hexahydrate (mass fraction of Mg based on CaO was 10%) were dissolved in an aqueous solution at room temperature with the molar ratio of Ca²⁺ to water as 1:40). Then, 7.5 g chelating agent of citric acid monohydrate was added under stirring. After mixing for **0.5 h**, Iron nitrate nonahydrate and cobalt nitrate hexahydrate with the total loading amount of 10 wt% corresponding to CaO were added into the mixture solution. Under vigorous stirring at 90 °C for 5 h, a transparent light-yellow sol was obtained. After the filtration, it was further dried at 120 °C overnight and calcined in a muffle furnace at 800 °C for 4 h with the heating rate of 2 °C min⁻¹. The obtained samples were denoted as **Fe_xCo_yMg₁₀CaO** (x, and y are the mass percentage of Fe and Co corresponding to CaO, respectively). **Fe₁₀Mg₁₀CaO** and **Co₁₀Mg₁₀CaO**, as well as pure CaO were also prepared as the reference samples. All the samples were crushed and compacted into fine pelleted particles of 40-50 mesh (0.35-0.45 mm or 10-20 mesh (0.85-2.0 mm) before the CO₂ capture and conversion test.

Characterization

The powder X-ray diffraction (PXRD) was carried out on a D/Max2550 VB/PC diffractometer (40 kV, 200 mA) using a Cu K α as the radiation. The morphology was characterized by a field-emission scanning electron microscope (FESEM, JEOL JEM-6360). The microstructure was characterized by a high-resolution transmission electron microscopy (HRTEM, a JEOL2010) with an elemental mapping. The porosity properties were determined by N₂ adsorption-desorption isotherms at 77 K on Micromeritics ASAP-3020, in which the Brunauer-Emmett-Teller (BET) model was used to calculate the specific surface area and the pore size distribution was calculated based on the Barrett-Joyner-Halenda approach. The elemental analyses were detected by an inductively coupled plasma atomic emission spectrometer (ICP, Varia 710 ES). The elemental states were determined by X-ray photoelectron spectroscopy (XPS, Thermo Fisher ESCALAB 250Xi).

Temperature-programmed-reduction with H₂ (H₂-TPR) was performed using an Autochem 2720 (equipped with thermal conductivity detector). In a typical experiment, a 100 mg sample was loaded in a quartz reactor and heated to 400 °C at the heating rate of 10 °C min⁻¹. After holding for 0.5 h

under 50 ml min⁻¹ nitrogen to remove moisture, the sample was heated again to 900 °C. The gas was switched into the gas mixture of H₂ and Ar (1:9 v/v) with the total flow rate of 50 ml min⁻¹. Temperature-programmed-desorption with CO₂ (CO₂-TPD) was also conducted using the same equipment. A 100 mg sample was pre-treated at 500 °C under the gas mixture of H₂ and N₂ (1:9 v/v) with a total flow rate of 50 ml min⁻¹ for a complete reduction. Subsequently, the sample was cooled to the room temperature, and exposed to the gas mixture of CO₂ and He (1:9 v/v) with a total flow rate of 50 ml min⁻¹ for 1h. Then, the gas was switched to He for 1.5 h to remove the physically adsorbed CO₂. Finally, the sample was heated to 900°C at the heating rate of 10 °C min⁻¹.

Mott-Schottky plots were recorded on an electrochemical workstation (Zahner, Zennium), which was conducted in a standard three-electrodes cell. The electrolyte was 0.5 mol L⁻¹ Na₂SO₄ aqueous solution. The working electrode was prepared by dropping 10 µL catalyst slurry (5 mg catalyst, 30 µL 5% Nafion dispersion, 666 µL deionized water, 333 µL isopropanol) on a glassy carbon electrode, and then dried at 80 °C for 30 min.

CO₂ Adsorption–Desorption

The fundamental CO₂ adsorption-desorption performance was determined through thermogravimetric analysis (TGA, Netzsch STA 449 F3 Jupiter). Firstly, the sample was heated to 500 °C under pure N₂ atmosphere for 0.5 h to remove the pre-adsorbed impurities. Then, raising the temperature to 650 °C, and the gas was switched to the gas mixture of CO₂ and N₂ (1:9 v/v) for adsorption. After 0.5 h, the adsorption was stopped by switching the gas back to pure N₂ or the mixture of H₂ and N₂ to start the desorption with the temperature kept unchanged for 0.5 h. The cyclic adsorption-desorption measurements were repeated at least for 10 times.

CO₂ capture and in-situ conversion

CO₂ capture and in-situ conversion were conducted in the same fixed-bed column (Scheme 1). The flow rates of N₂, CO₂, H₂ were controlled by the mass flow controllers (Horiba Metron). The products in the outlet gas were recognized by the Gas chromatography (GC, Haixin 950) and a nondispersive infrared analyser (Smart Pro, Shandon) was used to monitor the concentrations of CO and CO₂ continuously. In a typical microscale experiment, approximately 250 mg Fe_xCo_yMg₁₀CaO (40-50 mesh) was added in the quartz tube (Φ10 mm × 150 mm) and then placed in the reactor furnace. The first step was the sample pre-reduction, which was carried out at 550 °C in pure H₂ at the flow rate of 50 ml min⁻¹ for 1h. The second step was the CO₂ capture, in which the gas switched to a simulated flue gas of 10 vol% CO₂ balanced with N₂ at 50ml min⁻¹ and at the specific temperature such as 600, 650 and 700 °C for 0.5 h. The third step was the purge. The pipeline was purged by pure N₂ for 5 min. The fourth step was the CO₂ conversion, in which the temperature was kept the same as in CO₂ capture, and the gas was switched to pure H₂ or the mixture of H₂ and N₂ with different molar ratios at the flow rate of 30 ml min⁻¹, CO₂ was

reduced into CO, and the sample was regenerated for the cyclic performance tests. The operation variables of the temperature, gas hourly space velocity (GHSV), H₂ concentration in the conversion step and switching time were optimized respectively.

In the scale-up experiment, a 25 g pelletized Fe₅Co₅Mg₁₀CaO (10-20 mesh) sample was packed in an enlarged fixed-bed column made of a standard quartz tube (Φ25 mm × 500 mm). The reactor tube was surrounded by a thermal furnace, with a K-type thermocouple inserted in the bed for the temperature feedback control. The inlet gas flow rate was controlled by the mass flow controller (Horiba Metron). The concentration monitoring methods were the same as above, and the similar CO₂ capture and in-situ conversion processes were conducted under the optimal operation conditions.

The CO₂ adsorption capacity was calculated by Eq.1

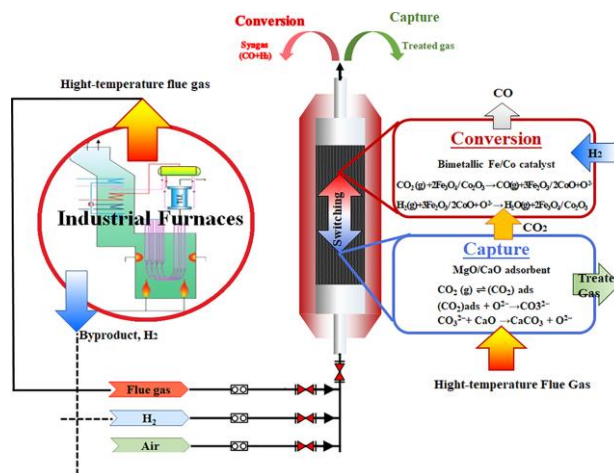
$$\text{CO}_2 \text{ sorption capacity (mmol g}^{-1}\text{)} = \left(\int_0^{t_s} [F_{\text{CO}_2}^{\text{in}} - F_{\text{CO}_2}^{\text{out}}(t)] dt \right) / M_0 \quad (1)$$

Where $F_{\text{CO}_2}^{\text{in}}$ (mmol min⁻¹) is the CO₂ molar flow rate in the inlet gas of the simulated flue gas, $F_{\text{CO}_2}^{\text{out}}$ (mmol min⁻¹) is the CO₂ molar flow rate in the outlet gas, t_s (min) is the duration time of capture, and M_0 (g) is the sample mass.

The CO₂ conversion efficiency was calculated by Eq.2

$$\text{CO}_2 \text{ conversion (\%)} = (n_{\text{CO}_2}^{\text{adsorbed}} - n_{\text{CO}_2}^{\text{unconverted}}) / n_{\text{CO}_2}^{\text{adsorbed}} \quad (2)$$

Where $n_{\text{CO}_2}^{\text{adsorbed}}$ (mol) is the amount of adsorbed CO₂ and $n_{\text{CO}_2}^{\text{unconverted}}$ (mol) is the amount of unconverted CO₂.



Scheme 1 The integration of CO₂ capture and in-situ conversion in one fixed-bed column with high-temperature industrial flue gas (for example, from ethylene manufacturing)

Results and discussion

Structure characteristics of Fe_xCo_yMg₁₀CaO

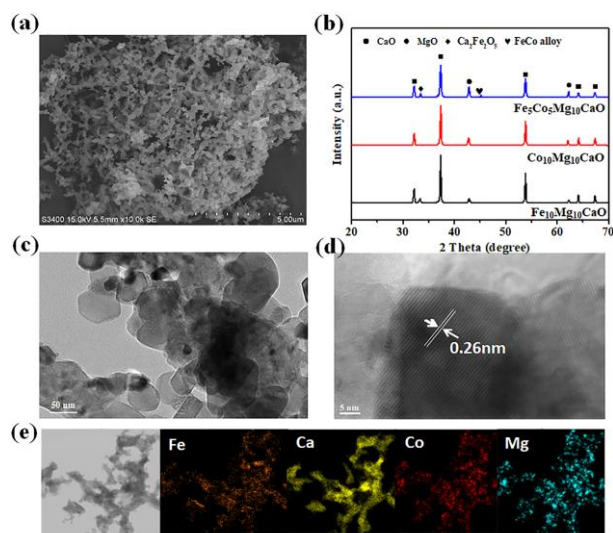


Figure 1 Characteristic properties of $\text{Fe}_5\text{Co}_5\text{Mg}_{10}\text{CaO}$ (a) SEM image (b) XRD patterns, (c) TEM image, (d) HR-TEM image, and (e) elemental mapping images

The obtained $\text{Fe}_x\text{Co}_y\text{Mg}_{10}\text{CaO}$ samples showed a three-dimensional branched coral-like morphology, consisting of the accumulated nanoparticles (Figure 1a and Fig. S1). The pore size distribution determined by the N_2 adsorption isotherms (Fig. S2) confirmed the hierarchical meso/macro-porous structures. The XRD patterns evidenced the presence of CaO (PDF# 48-1467) and MgO (PDF#45-0946) crystals, but without any diffraction peaks of Fe or Co oxides, suggesting the highly dispersed Fe and Co in CaO (Figure 1b and Fig. S3). Based on the characteristic peak of CaO at 37.36° , the crystal size of CaO, calculated by the Scherrer equation, was about 28.3 nm in $\text{Fe}_5\text{Co}_5\text{Mg}_{10}\text{CaO}$, much smaller than 38.4 nm and 33.6 nm in $\text{Fe}_{10}\text{Mg}_{10}\text{CaO}$ and $\text{Co}_{10}\text{Mg}_{10}\text{CaO}$, respectively (Table S1). It is worth mentioning that there was a small diffraction peak at 33.5° in both XRD patterns of $\text{Fe}_5\text{Co}_5\text{Mg}_{10}\text{CaO}$ and $\text{Fe}_{10}\text{Mg}_{10}\text{CaO}$, which was ascribed to the characteristic peak of $\text{Ca}_2\text{Fe}_2\text{O}_5$,⁴⁸ suggesting the melt-intercalation of Fe into CaO during the high-temperature calcination. Moreover, a small diffraction peak at 44.9° , ascribed to the characteristic peak of Fe-Co alloy, was observed in the XRD pattern of $\text{Fe}_5\text{Co}_5\text{Mg}_{10}\text{CaO}$, which could provide a synergistic catalytic effect for the CO_2 conversion. From the transmission electron microscopy (TEM) image of $\text{Fe}_5\text{Co}_5\text{Mg}_{10}\text{CaO}$ (Figure 1c), some hexagonal CaO particles with the size of about 50 nm were observed, but most of them were irregular aggregations. In addition, there are some small dark crystal particles distributed on the surface. With the spacing of the lattice fringe of 0.26 nm, it was assigned to the (141) face of $\text{Ca}_2\text{Fe}_2\text{O}_5$ crystal⁴⁹(Figure 1d). The elemental mapping images of $\text{Fe}_5\text{Co}_5\text{Mg}_{10}\text{CaO}$ further demonstrated the uniform distributions of Ca, Mg, Fe and Co elements (Figure 1e), which could effectively prevent CaO sintering, resulting in an excellent stability in the following cyclic CO_2 capture tests. Moreover, the ICP-OES results showed the contents of Ca, Mg, Fe and Co elements in $\text{Fe}_x\text{Co}_y\text{Mg}_{10}\text{CaO}$ were all in consistent with predetermined mass fractions (Table S1).

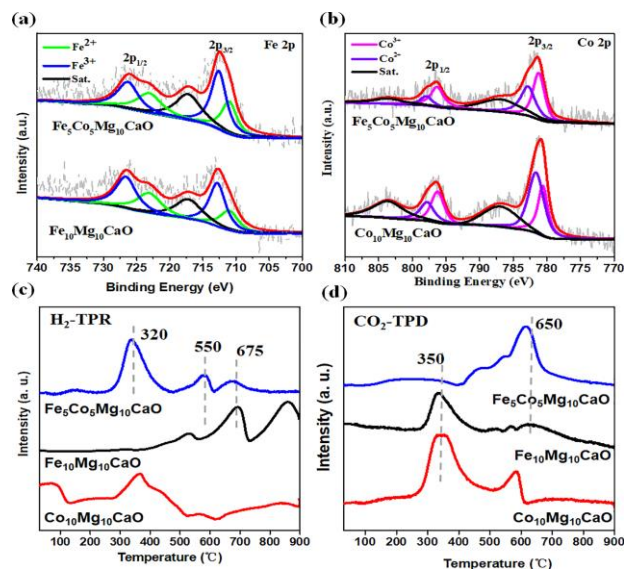


Figure 2 High-resolution XPS spectra of (a) Fe 2p of $\text{Fe}_5\text{Co}_5\text{Mg}_{10}\text{CaO}$ and $\text{Fe}_{10}\text{Mg}_{10}\text{CaO}$, and (b) Co 2p of $\text{Fe}_5\text{Co}_5\text{Mg}_{10}\text{CaO}$ and $\text{Co}_{10}\text{Mg}_{10}\text{CaO}$; (c) H_2 -TPR patterns and (d) CO_2 -TPD patterns of $\text{Fe}_x\text{Co}_y\text{Mg}_{10}\text{CaO}$

As Fe and Co oxides showed no characteristic XRD peaks, we adopted XPS to determine their valence states in $\text{Fe}_x\text{Co}_y\text{Mg}_{10}\text{CaO}$. The XPS spectrum of the elemental survey scan exhibited typical peaks of Ca, Mg, Fe, Co respectively (Fig. S4a). Based on the high resolution Fe and Co 2p spectra, $\text{Fe}^{3+}/\text{Fe}^{2+}$ and $\text{Co}^{3+}/\text{Co}^{2+}$ turned out to be the predominant valences in the $\text{Fe}_5\text{Co}_5\text{Mg}_{10}\text{CaO}$ (Figure 2a and 2b)^{50, 51}. In comparison with monometallic $\text{Fe}_{10}\text{Mg}_{10}\text{CaO}$ and $\text{Co}_{10}\text{Mg}_{10}\text{CaO}$, the binding energy of Fe^{2+} and Fe^{3+} showed a negative shift of 0.3 eV and 0.6 eV; whereas that of Co^{2+} and Co^{3+} showed a positive shift of +0.4 eV and +0.2 eV, respectively (Table S2), suggesting Fe-Co forming an alloy through the electron-transfer from Co to Fe. Moreover, the Ca 2p spectrum shifted a little to higher binding energy of 346.57 eV ($2p_{3/2}$) and 350.07 eV ($2p_{1/2}$), respectively (Fig. S4b). With a binding energy difference of 3.5 eV and a half peak intensity ratio, it indicated Ca^{2+} was in an excited state,⁵² and the formation of $\text{Ca}_2\text{Fe}_2\text{O}_5$ by the melt-intercalation was further confirmed.

The activity of metal-based catalysts for the RWGS reaction is more likely related to its redox reaction. Comparing with the H_2 -TPR patterns of monometallic $\text{Co}_{10}\text{Mg}_{10}\text{CaO}$ and $\text{Fe}_{10}\text{Mg}_{10}\text{CaO}$ catalysts, the bimetallic $\text{Fe}_5\text{Co}_5\text{Mg}_{10}\text{CaO}$ showed three reduction peaks (Figure 2c), of which the first one at 320°C was ascribed to the reduction of Co^{3+} to Co^{2+} ; whereas the second and third ones, attributed to the reduction of Fe^{3+} to Fe^{2+} , shifted towards much lower temperature of 550°C and 675°C from 675°C and 850°C of $\text{Fe}_{10}\text{Mg}_{10}\text{CaO}$, suggesting the catalytic reduction activity of $\text{Fe}_5\text{Co}_5\text{Mg}_{10}\text{CaO}$ was significantly improved. In addition, it had been demonstrated the mixed phase of $\text{Ca}_2\text{Fe}_2\text{O}_5$ and Fe_2O_3 had an excellent activity for the hydrogen production in toluene steam reforming,⁵³ therefore, the catalytic activity of $\text{Fe}_5\text{Co}_5\text{Mg}_{10}\text{CaO}$ could be also suitable for the RWGS reaction. While in the CO_2 -TPD tests (Figure 2d), $\text{Fe}_5\text{Co}_5\text{Mg}_{10}\text{CaO}$ showed a strong peak at 650°C , higher than the main peak of $\text{Fe}_{10}\text{Mg}_{10}\text{CaO}$ and $\text{Co}_{10}\text{Mg}_{10}\text{CaO}$ at 350°C and

small peak at about 600 °C, revealing the bimetallic Fe/Co doping effectively increased the CO₂ affinity of CaO, which would endow its excellent CO₂ capture capability.

CO₂ adsorption performance

The CO₂ adsorption performance of **Fe_xCo_yMg₁₀CaO** from a simulated flue gas (the molar ratio of CO₂: N₂=1:9) through the CaL over a wide temperature range of 30 °C to 900 °C was recorded by monitoring the CO₂ concentration in the outlet gas (Figure 3a and Fig. S5). When the temperature was increased to 300 °C, a small peak appeared, attributed to the CO₂ adsorption on MgO. However, further increasing the temperature resulted in the CO₂ desorption due to the decomposition of MgCO₃. When the temperature was above 400 °C, the CO₂ adsorption took place again on CaO. In line with the thermodynamic characteristics of high-temperature CO₂ capture by CaO, the CO₂ adsorption rate reached the maximum when the temperature was about 650 °C. Further increasing the temperature caused a fast decrease in CO₂ adsorption rate due to the decomposition of CaCO₃. Thus, the temperature of CO₂ capture was fixed at 650 °C to investigate the adsorption performance of **Fe_xCo_yMg₁₀CaO** and **CaO** (Figure 3b and Fig. S6). Data processing through fitting the Langmuir model to the adsorption isotherms and the pseudo-second-order kinetic law to the dynamic adsorption curves at 650 °C gave results as shown in Fig. S6 and Table S3. Fe₅Co₅Mg₁₀CaO exhibited the best adsorption performance among all the samples, with CO₂ adsorption equilibrium capacity of 9.93 mmol g⁻¹ and the rate constant of 0.1064 g mmol⁻¹ min⁻¹.

The CO₂ desorption performance was also investigated by the purge of pure N₂ and the mixture of H₂ and N₂ (with the molar ratio of 1:9), respectively. For **Fe₅Co₅Mg₁₀CaO**, the CO₂ desorption started at 650 °C in the purge of pure N₂ (Fig. S7). Whereas adding 10 vol% H₂ balanced with N₂, it started at a lower temperature of 610 °C. More significantly, carbon monoxide was produced at even lower temperature of 550 °C

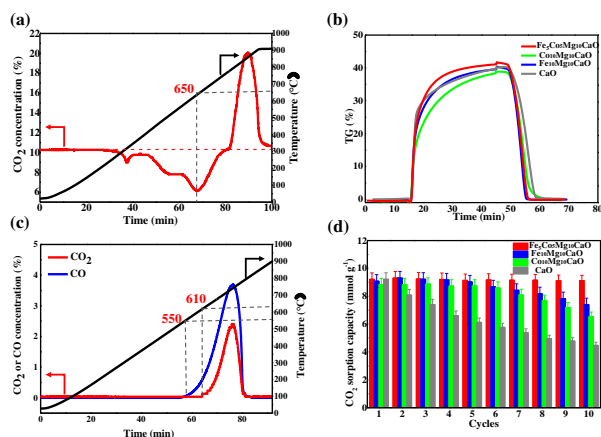


Figure 3 CO₂ capture from a simulated flue gas (10 vol% CO₂) through CaL (a) dynamic changes of CO₂ concentration in the outlet gas in the temperature range of 30 °C to 900 °C on **Fe₅Co₅Mg₁₀CaO**; (b) CO₂ capture dynamic profiles of **Fe_xCo_yMg₁₀CaO** and **CaO** at 650 °C; (c) CO₂ desorption performance on **Fe₅Co₅Mg₁₀CaO** purged by the 10 vol% H₂ balanced with N₂; (d) Comparison of cyclic CO₂ adsorption-desorption stability on **Fe_xCo_yMg₁₀CaO** and **CaO** at 650 °C.

(Figure 3c). Therefore, when H₂ was used as the purging gas, not only a faster regeneration of CaCO₃ to CaO at a lower temperature, but also a CO₂ conversion to CO was achieved. This desorption performance provided a clear evidence that the CO₂ capture and the in-situ conversion could take place successively in a same column.

Ten cycle tests of CO₂ adsorption-desorption at 650 °C in N₂ purge using TGA further revealed higher stability of **Fe_xCo_yMg₁₀CaO** than pure CaO (Figure 3d and Fig. S8). Among them, **Fe₅Co₅Mg₁₀CaO** showed the best stability, with the capacity maintaining > 95%. Only a small decline from 9.58 mmol g⁻¹ to 9.20 mmol g⁻¹ was observed, much better than **Fe₁₀Mg₁₀CaO** (from 9.09 mmol g⁻¹ to 7.41 mmol g⁻¹) and **Co₁₀Mg₁₀CaO** (from 8.90 mmol g⁻¹ to 6.68 mmol g⁻¹), suggesting the serious problem of the CaO sintering was successfully overcome by the porous structure and the hybrid doping of Mg, Fe, Co oxides.

Integration CO₂ capture with in-situ conversion

The integration of CO₂ capture and in-situ conversion process was studied experimentally in the same fixed bed column (Scheme 1), which consisted of three steps (Figure 4a): the CO₂ capture, the purge and the conversion. After the adsorption, the simulated flue gas was switched to pure N₂ to purge the residual gases in pipeline, then it was switched to pure H₂ for the CO₂ reduction. Firstly, we focused on the most important issue of temperature matching between the CaL for CO₂ capture and the RWGS reaction for CO₂ conversion (Figure 4b). In the temperature range of 600 °C to 700 °C, the CaL of **Fe₅Co₅Mg₁₀CaO** showed an optimal CO₂ capacity of 9.2 mmol g⁻¹ at 650 °C; meanwhile, the RWGS reaction rate increased with the temperature below 650 °C, with the CO₂ conversion efficiency maintaining above 90%. However, the CO₂ conversion efficiency sharply decreased to 77.4% at 700 °C since the RWGS reaction could not catch up the fast CaCO₃ decomposition at the excessively high temperature.

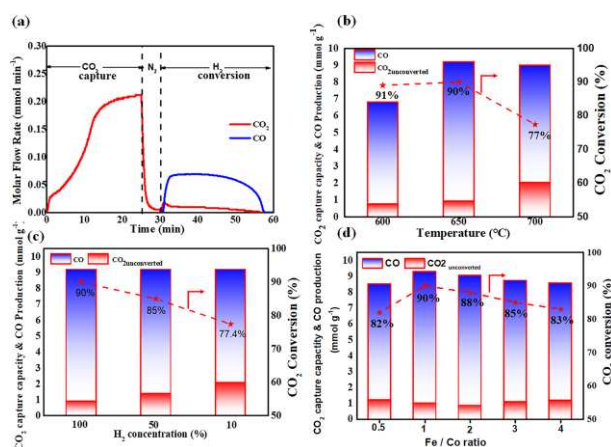


Figure 4 (a) Integration of CO₂ capture and conversion process at 650 °C on **Fe₅Co₅Mg₁₀CaO**, at flow rate of 50 ml min⁻¹; (b) Temperature effect on CO₂ capture capacity and subsequent conversion efficiency; (c) The effect of H₂ content on the conversion efficiency at 650 °C; (d) the effect of Fe/Co ratios in **Fe_xCo_yMg₁₀CaO** on the CO₂ capture capacity and the in-situ conversion efficiency under the optimal operating conditions.

Table 1 The integrated CO₂ capture and conversion performance of different adsorbent/catalysts **Fe_xCo_yMg₁₀CaO** at 650 °C.

Samples	CO ₂ capacity (mmol g ⁻¹)	CO ₂ unconverted (mmol g ⁻¹)	CO yield (mmol g ⁻¹)	^a Carbon balances (%)	CO ₂ conversion (%)
CaO	9.2	2.76	2.76	60.0	50
Fe ₁₀ Mg ₁₀ CaO	9.09	1.80	7.20	99.0	80
Fe ₈ Co ₂ Mg ₁₀ CaO	8.9	1.36	7.10	96.2	83
Fe _{7.5} Co _{2.5} Mg ₁₀ CaO	9.0	1.31	7.42	97.0	85
Fe _{6.7} Co _{3.3} Mg ₁₀ CaO	9.3	1.08	7.95	97.2	88
Fe ₅ Co ₅ Mg ₁₀ CaO	9.2	0.92	8.28	100	90
Fe _{3.3} Co _{6.7} Mg ₁₀ CaO	8.9	1.53	6.97	95.5	82
Co ₁₀ Mg ₁₀ CaO	8.9	2.18	6.54	98.0	75

^a Carbon balance = (CO yield + CO₂ unconverted)/captured CO₂

Considering the overall efficiencies in both steps of CO₂ capture and conversion, the optimal temperature was set at 650 °C. In addition, the H₂ content and gas-volume hourly space velocity (GHSV) of the inlet gas at the conversion stage were also investigated. The CO₂ conversion efficiency increased almost linearly with the H₂ content in the inlet gas, from 77.4% in 10 vol% H₂ to 90% in pure H₂ (Figure 4c). Moreover, the higher the H₂ content, the shorter the conversion time (Fig. S9a). Since the CO₂ desorption rate and conversion rate are strongly related to the GHSV of H₂, with the total CO₂ conversion kept similarly at about 90%, it took 67 min, 42 min and 32 min to convert the adsorbed CO₂ into CO when GHSV was 1910 h⁻¹, 3820 h⁻¹, and 5730 h⁻¹, respectively (Fig. S9b). With the similar CO conversion efficiency, the higher GHSV, the faster desorption and RWGS reaction rate. Therefore, a suitable GHSV of H₂ around pre-adsorbed CO₂ is necessary for effective in-situ conversion.

Specifically, under the optimal operating conditions (i.e. the temperature at 650 °C and the GHSV at 5730 h⁻¹ in pure H₂), more samples of **Fe_xCo_yMg₁₀CaO** with different Fe/Co mass ratios of 0.5, 1, 2, 3, and 4 were tested. As listed in Table 1, **Fe_xCo_yMg₁₀CaO** all exhibited excellent CO₂ adsorption capacity in the range of 8.9–9.3 mmol g⁻¹, comparable with the pure fresh CaO (9.2 mmol g⁻¹). Meanwhile, their CO₂ conversion efficiency were different in the range of 82%–90%, better than that of either monometallic catalyst of **Fe₁₀Mg₁₀CaO** or **Co₁₀Mg₁₀CaO** (Figure 4d). Among them, **Fe₅Co₅Mg₁₀CaO** showed the highest

efficiency of 90% with the CO yield of 8.28 mmol g⁻¹. As only a trace of CH₄ (yield < 0.03%) was detected in the outlet, CO₂ was almost completely converted into CO with the selectivity close to 100%. Moreover, **Fe₅Co₅Mg₁₀CaO** showed the fastest conversion rate of 0.08 mmol min⁻¹ (Fig. S10). These results provided a clear evidence that the bimetallic Fe/Co doping catalyst synergistically enhanced the catalytic conversion. Compared with state-of-the-art reported work (Table S4), with the CO₂ conversion efficiency of 90% and almost 100% CO selectivity, **Fe₅Co₅Mg₁₀CaO** showed the highest CO₂ conversion efficiency so far to the best of our knowledge.

Cycling tests for CO₂ capture and in-situ conversion stability

To explore the stability of CO₂ capture and in-situ conversion performance, 10 successive runs at 650 °C in one fixed-bed column were examined. With the flue gas flow rate at 50 ml min⁻¹, **Fe₅Co₅Mg₁₀CaO** (250 mg, 40–50 mesh) showed an excellent stability with the adsorption capacity kept as high as 9.20 mmol g⁻¹, the CO₂ conversion maintained at about 90% and the CO yield of 8.28 mmol g⁻¹ (Figure 5). The SEM image of **Fe₅Co₅Mg₁₀CaO** after 10 cycles confirmed its stable porous structure (Fig. S11a), revealing the hybrid doping of Mg, Fe, Co oxides has a synergistic effect to prevent CaO sintering. Moreover, comparing with the XRD pattern of the fresh **Fe₅Co₅Mg₁₀CaO**, it showed almost no change after 10 cycle runs, except for the appearance of a peak of Ca(OH)₂ (Fig. S11b), suggesting that the highly dispersed Fe/Co catalysts in porous CaO assured their catalytic stability.

Heterojunction-Redox mechanism of bimetallic catalysts for the adsorption enhanced in-situ conversion

The structure contribution of this bimetallic **Fe₅Co₅Mg₁₀CaO** was further illustrated to understand the mechanism for its excellent performance of simultaneous CO₂ capture and conversion (Scheme 2). Comparing with the XPS spectra of fresh **Fe₅Co₅Mg₁₀CaO**, the characteristic peaks in the high-resolution Ca 2p, Fe 2p and Co 2p spectra all showed

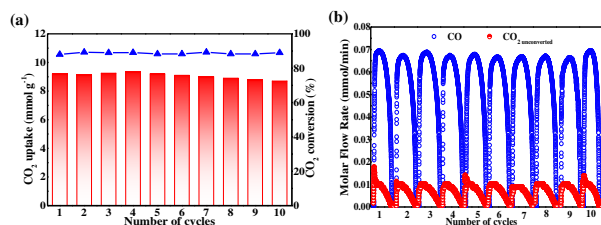
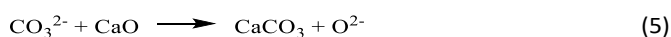
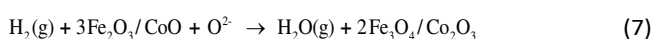
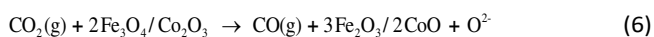


Figure 5 10 cyclic CO₂ capture and in-situ conversion performance of **Fe₅Co₅Mg₁₀CaO** at 650 °C in one fixed-bed column (a) CO₂ capture capacity (mmol g⁻¹) and conversion efficiency (%) (b) the molar flow rate of CO and CO₂ in the outlet gas after the conversion

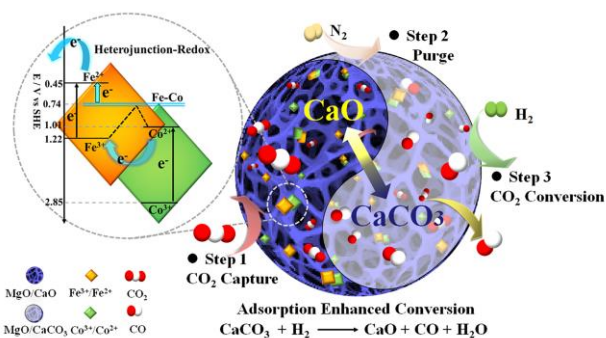
negative shifts after the CO₂ adsorption (Fig S12, Table S5 and S6), indicating Fe and Co also participated in the CO₂ adsorption. Moreover, O1s spectra exhibited abundant of O²⁻ species (O2, ~531.2 eV) in the fresh Fe₅Co₅Mg₁₀CaO for CO₂ adsorption.⁵⁴ After the adsorption, it showed a significant decrease; whereas an increase of the metal-oxygen bond (O3, 529.5 eV) was observed. Therefore, in the first stage of CO₂ capture, the structure of Fe₅Co₅Mg₁₀CaO provides great advantages during the CaL including (1) The hierarchical porous structure not only provides conducive channels for rapid CO₂ diffusion, but also large surface area for the surface adsorption; (2) as O²⁻ has been assigned to the active site for CO₂ adsorption in the CaL process (Eq. 3-5),⁵⁵ the presence of different valence states of doped Fe and Co oxides provides extra oxygen vacancies to facilitate the CO₂ adsorption;⁵⁶ (3) the melt-intercalation of Fe₂O₃ into CaO through the high-temperature calcination and the high-temperature refractory of MgO successfully prevents CaO sintering, high stability is achieved.



After the conversion, a further negative shift of Fe 2p high resolution XPS spectrum was observed, and the mass ratio of Fe²⁺/Fe³⁺ increased from 0.47 to 0.75. While no obvious shift was observed in the Co 2p spectrum, the mass ratio of Co²⁺/Co³⁺ maintained at about 1.6. (Fig. S12 and Table S7) Thus, Fe²⁺ was demonstrated to be the active catalytic sites, whereas Co acted as the catalytic promoter in Fe₅Co₅Mg₁₀CaO. They synergistically facilitated the electron donation through the heterojunction redox mechanism to promote the CO₂ reduction. Therefore, in the second stage of CO₂ conversion through the RWGS reaction (Eqs. 6 and 7), firstly, CO₂ was catalytically reduced to CO by the magnetite (Fe₃O₄).³⁸ Secondly, the hematite (Fe₂O₃) was regenerated by H₂ under the promoter of Co.⁵⁷ During this process, the pre-adsorbed CO₂ significantly enhanced the following in-situ conversion because (1) the highly dispersed Fe or Co-oxides facilitates the catalytic RWGS reaction with the adsorbed CO₂ nearby, especially for those at the oxygen vacancies of Fe and Co oxides; (2) the fresh CO₂ adsorbed on CaO in H₂ atmosphere is more reductive, this adsorption enhanced conversion (AEC) effect greatly improves the conversion efficiency and CO selectivity.



Inspired by the photocatalytic mechanism, we further proposed the heterojunction-redox mechanism (Scheme 2) to understand this bimetallic catalytic RWGS reaction. In Fe₅Co₅Mg₁₀CaO, the electrons hopping between the redox couples of Fe²⁺ and Fe³⁺ (with the standard redox potential of 0.77 V) are dominant active sites (Eq. 8), whereas the redox



Scheme 2 Heterojunction-redox mechanism of bimetallic catalyst Fe₅Co₅Mg₁₀CaO for the adsorption enhanced in-situ conversion

couple of Co²⁺ and Co³⁺ (1.92 V) is a promotor (Eq.9). Determined from the Mott-Schottky plots (Fig. S13),⁵⁸ the flat-band potentials (E_{FB}) of Fe₅Co₅Mg₁₀CaO, Fe₁₀Mg₁₀CaO, and Co₁₀Mg₁₀CaO were ca. 0.50 V, 0.21 V, and 0.77 V respectively. As the Fermi level potential (E_{F}) can be roughly estimated by $E_{\text{F}}(\text{V}) = E_{\text{FB}} + 0.24$, where 0.24 V is the electric potential of saturated HgCl₂/Hg₂Cl₂ electrode vs. Standard Hydrogen Electrode,^{59, 60} the E_{F} of Fe₅Co₅Mg₁₀CaO, Fe₁₀Mg₁₀CaO and Co₁₀Mg₁₀CaO were ca. 0.74 V, 0.45 V and 1.01 V respectively, suggesting an internal electric field formed in Fe³⁺/Fe²⁺ and Co³⁺/Co²⁺ redox couples until a new Fermi level of Fe₅Co₅Mg₁₀CaO reached equilibrium, which is a characteristic of heterojunction. Because of the synergistic effect of Fe/Co in which Co transferred electron to Fe, newly formed Fermi level of Fe-Co alloy makes it easier for electrons spilled-over to facilitate the heterojunction-redox catalysis.^{61, 62} Moreover, the Fermi level of Fe₅Co₅Mg₁₀CaO heterojunctions (0.74 V) is much higher than the electric potential of CO₂/CO (-0.52 V),⁶³ the adsorbed CO₂ molecules around the active bimetallic catalytic-sites are easily reduced to CO (Scheme 2). Therefore, the synergistic heterojunction-redox between the bimetallic couples could be responsible for the improved RWGS reaction activity, which provides a promising strategy to design bimetallic catalysts.



Scale-up study

Since the scalability is a crucial criterion for commercial deployment of the proposed technology, the scale-up experiment was carried out to investigate the effect of key parameters such as the reactor geometry, the catalyst size, the flow rate of the flue gas and H₂, and time matching between capture and conversion. Compared with the above microscale experiments of 250 mg Fe₅Co₅Mg₁₀CaO (40-50 mesh) packed in the column (Φ10 mm × 150 mm), 25 g pelletized Fe₅Co₅Mg₁₀CaO at 10-20 mesh was packed in the column (Φ25 mm × 500 mm) (Figure 6a and 6b, Table S8). The temperature of both CO₂ capture and in-situ conversion were still set at 650 °C. When the flow rate of the simulated flue gas (10 vol% CO₂)

Table 2 Economic evaluation of the operation costs of the integrated CaL/RWGS process.

Operation costs (million \$ /yr)					
Utility cost		CO ₂ tax ^a		Feed	
Nature gas	1.72	CO ₂ in feed	-0.7	H ₂	12.5
electricity	2.16	Nature gas ^b	0.24	Flue gas (CO ₂) ^c	0
				Fe ₅ Co ₅ Mg ₁₀ CaO	0.58
Total	3.88	Total	-0.46	Total	13.08
Total operation cost: \$16.5×10 ⁶ /yr					
Operation cost of CO ₂ avoided: \$165/tCO ₂					

^a a CO₂ tax credit is given to the integrated CaL/RWGS process for consuming CO₂ as a raw material.

^b CO₂ tax by burning natural gas and the emission of 0.00164 kmol s⁻¹ of CO₂ to generate 1 MW of energy in the form of heat.⁶⁴

^c CO₂ is assumed to be free as a raw material.

was controlled at 200, 500, 1000, and 2000 ml min⁻¹, the CO₂ adsorption curves showed a breakthrough at 260, 125, 25 and 10 min respectively (Fig. S14). Among them, with almost 50 times enlarged in total throughput of the simulated flue gas at the flow rate of 500 ml min⁻¹, the CO₂ capture capacity still maintained as high as 9.10 mmol g⁻¹ (Table S9). After the purge, the inlet gas was switched into pure H₂ at the same flow rate of 500 ml min⁻¹, the in-situ CO₂ conversion was completed within 90 min, i.e. only 3 times longer than the microscale one. The CO₂ conversion efficiency showed only a small decrease but still as high as 87%, with the CO selectivity of 100% (Figure 6c, Table S9). Moreover, a stable performance in 10 cycle runs further demonstrated the stability of this integrated CaL/RWGS technology (Figure 6d). Therefore, the key parameters can be effectively controlled during the scale-up.

To study the scalability of the proposed technology at the commercial scale, we carried out further scale-up using

computer modelling and simulation through gPROMS MobilBuilder[®]. For a commercial plant producing 100,000 t/yr ethylene from naphtha, we set the flue gas flow rate as 10 m/s and its temperature around 650 °C. A fixed-bed reactor with 2.5 m (internal diameter) and 10 m (length) is required to hold 50 t Fe₅Co₅Mg₁₀CaO. When the CO₂ capture capacity and the capture efficiency are set as 9 mol kg⁻¹ and 95%, 19.5 t CO₂ will be captured with breakthrough time at 7,200 seconds in one run (Fig. S15). Then the feed gas is switched to pure H₂ with the flow rate at 1 m s⁻¹ at 650 °C. H₂ reacts with the adsorbed CO₂ to produce CO immediately. CO₂ conversion efficiency reaches 90% with CO selectivity at 100% and holds almost constant after 10 cycles (Fig.S16). For more details, please refer to the supplementary information.

Economic evaluation

To evaluate the economic benefits of the proposed integrated CaL/RWGS technology, we integrated this high-temperature CO₂ capture and in-situ conversion process with a 100,000 t/yr ethylene plant (Fig. S17). The yearly operating time is assumed to be 8,000 hours. The flow rate of the flue gas from such an ethylene plant (at 10 vol% CO₂) was calculated to be 8.4 × 10⁴ kg h⁻¹. Based on the temperature profile of the thermal cracking furnace of the ethylene plant, the flue gas with the temperature of 650 °C was directed into the fixed-bed column reactor. Based on the simulation results, 50 t Fe₅Co₅Mg₁₀CaO was filled in the column (Φ2,5 m × 10 m). The integrated CaL/RWGS process takes place in turn inside the same column at 650 °C, with the CO₂ adsorption capacity of 9 mol/kg; the CO₂ conversion efficiency was set as 85% (5% decreases for the unforeseen circumstances) and CO selectivity of 100%. Accordingly, the material flows and the energy flows (per hour) in each step during the integrated CaL/RGWR process (Table S10) were calculated. Without any additional desorption process, Fe₅Co₅Mg₁₀CaO is regenerated for the next cycle of CO₂ capture and conversion.

The economic evaluation based on the pricing in China (Fig. S18, Table S11) shows that the operation costs are dominated by the cost of H₂ feed (\$12.5 million/yr) and Fe₅Co₅Mg₁₀CaO (\$0.58 million/yr), electricity for blowers and heating (\$2.16 million/yr), and natural gas for heating (\$1.72 million/yr) (Table 2). Among them, H₂ is the cost-determining factor. Fortunately, H₂ is also a by-product in the ethylene

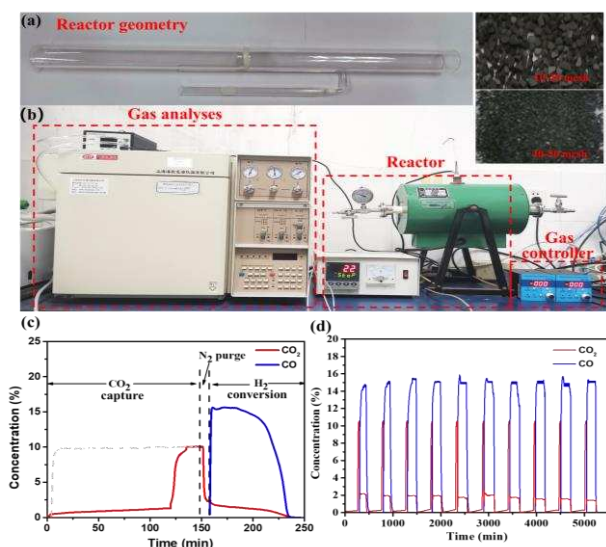


Fig. 6 (a) comparison of the reactor geometry and catalyst size between the microscale and the scale-up experiments, (b) the scale-up system of the integrated CO₂ capture and conversion reactor (with the reactor column (Φ25 mm × 500 mm)). The scale-up experiment results of integrated CO₂ capture and conversion processes on 25 g Fe₅Co₅Mg₁₀CaO at 650 °C (c) concentration profiles at the flow rate of 500 ml min⁻¹ and (d) 10 cycles stability at the flow rate of 200 ml min⁻¹.

plant, accounting for about 1-2% of the total output. Then the cost of 2,000 -4,000 t/yr H₂ can be saved.⁶⁵ As a result, the operation cost for the integrated CaL/RWGS process is about \$165/t(CO₂), much lower than the reported \$323/t(CO₂) of the individual RWGS conversion (syngas production) with CO₂ and H₂ as the reactant, in which H₂ is produced by the water split.³⁹ In addition, the operation cost of the CaL process for CO₂ capture was reported as \$70/t(CO₂).⁶⁶ It is worth mentioning that for a conventional CCUS, CO₂ needs to be compressed and transported after the capture. It has been reported the cost of CO₂ transportation is at least \$20/t(CO₂) and this does not include the huge capital costs of the pipeline network and collecting system.⁶⁷ If we simply combine two reported separated processes of CaL and RWGS conversion together, the operation cost will be at least \$393/t(CO₂), which is 138% higher than this integrated CaL/RWGS process. Moreover, as the outlet gas of this integrated CaL/RWGS process consists of about 67 vol% of unreacted H₂ and the converted CO with the molar ratio of 2:1, it can be a source of the syngas for the downstream conversion to produce valuable chemicals and fuels such as methanol through the Fischer-Tropsch synthesis.⁶⁸ If we take this into account, then this integrated CaL/RWGS technology will produce additional \$9.38 million/yr profit (Table 2 and Table S11). More importantly, with the CO₂ capture and conversion taking place in the same column, it will save capital costs significantly, which we have not quantified in this study.

Conclusions

A novel bifunctional adsorbent/catalyst **Fe₅Co₅Mg₁₀CaO** was synthesized for CO₂ capture and in-situ conversion. With the high-temperature refractory of MgO and the highly dispersed Fe and Co oxides in the hierarchical porous CaO, the bottle-neck problem of CaO sintering in CaL was successfully solved. Moreover, the presence of different valence states of doped Fe and Co oxides provides extra oxygen vacancies to facilitate the CO₂ adsorption. As a result, a stable high-temperature CO₂ capture capacity of 9.0-9.2 mmol g⁻¹ was achieved. After optimizing the operating conditions, two separate processes of CaL and RWGS reaction were integrated in one fixed-bed column operating at the same temperature of 650 °C. Attributed to the adsorption enhanced conversion effect, the in-situ CO₂ conversion was nearly 90% and the CO selectivity is close to 100%. More significantly, the heterojunction-redox mechanism was proposed for the first time to illustrate the synergistic effect of the bimetallic Fe³⁺/Fe²⁺ and Co³⁺/Co²⁺ redox couples through the newly formed Fermi level in **Fe₅Co₅Mg₁₀CaO**. The scaled-up studies from gram level to large scale commercial deployment for 100,000 t/yr ethylene plant through experiments and computer simulation further demonstrate the stable scalability of this integrated CaL/RWGS technology. The economic analysis reveals that the operation cost using the newly proposed integrated technology stands at \$165/tCO₂. The operating cost for separated CaL and RWGS process will be at least \$393/tCO₂, which is 138% higher than the newly proposed technology. Therefore, the hybrid doping of bimetallic Fe/Co in porous CaO provides a promising strategy

for designing the bifunctional adsorbent/catalyst materials. Accordingly, an efficient, energy-saving and cost-effective adsorption enhance conversion technology for simultaneous CO₂ capture and utilization was successfully achieved for green manufacturing.

Conflicts of interest

There are no conflicts to declare.

Acknowledgements

We appreciate the helpful suggestions and comments from Professors Xingui Zhou and Jing Xu at ECUST, and Professor Xiangping Zhang at Institute of process engineering, Chinese Academy of Sciences (CAS).

Financial support from Shanghai Science and Technology Committee (No. 19160712100), EU RISE project (No. 101007963), National Natural Science Foundation of China (Basic Science Centre Program: 61988101) and the Natural Science Foundation of China (Nos. 21676080 and 21878076) are acknowledged.

References

- B. J. Strengers, J. G. Van Minnen and B. Eickhout, *Climatic Change*, 2008, **88**, 343-366.
- E. A. Quadrelli, G. Centi, J. L. Duplan and S. Perathoner, *Chemsuschem*, 2011, **4**, 1194-1215.
- M. Peters, B. Kohler, W. Kuckshinrichs, W. Leitner, P. Markewitz and T. E. Muller, *Chemsuschem*, 2011, **4**, 1216-1240.
- D. P. Hanak, E. J. Anthony and V. Manovic, *Energy Environ. Sci.*, 2015, **8**, 2199-2249.
- Z. Yuan, M. R. Eden and R. Gani, *Ind. Eng. Chem. Res.*, 2015, **55**, 3383-3419.
- D. Y. C. Leung, G. Caramanna and M. M. Maroto-Valer, *Renewable Sustainable Energy Rev.*, 2014, **39**, 426-443.
- M. Bui, C. S. Adjiman, A. Bardow, E. J. Anthony, A. Boston, S. Brown, P. S. Fennell, S. Fuss, A. Galindo, L. A. Hackett, J. P. Hallett, H. J. Herzog, G. Jackson, J. Kemper, S. Krevor, G. C. Maitland, M. Matuszewski, I. S. Metcalfe, C. Petit, G. Puxty, J. Reimer, D. M. Reiner, E. S. Rubin, S. A. Scott, N. Shah, B. Smit, J. P. M. Trusler, P. Webley, J. Wilcox and N. Mac Dowell, *Energy Environ. Sci.*, 2018, **11**, 1062-1176.
- O. Edenhofer, R. Pichs-Madruga, Y. Sokona, E. Farahani, S. Kadner, K., A. A. Seyboth, I. Baum, S. Brunner, P. Eickemeier, B. Kriemann, J. Savolainen, S. Schlömer, C. von Stechow, T. Zwickel and J.C. and M. (eds.), 2014, IPCC, 2014: Climate Change 2014: Mitigation of Climate Change. Contribution of Working Group III to the Fifth Assessment Report of the Intergovernmental Panel on Climate Change, Cambridge University Press, Cambridge, United Kingdom and New York, NY, USA.
- J. M. Bielicki, R. S. Middleton, J. S. Levine and P. Stauffer, *Energy Procedia*, 2014, **63**, 7215-7224.
- G. Qi, Y. Wang, L. Estevez, X. Duan, N. Anako, A.-H. A. Park, W. Li, C. W. Jones and E. P. Giannelis, *Energy Environ. Sci.*, 2011, **4**, 444-452.

11. J. Wang, L. Huang, R. Yang, Z. Zhang, J. Wu, Y. Gao, Q. Wang, D. O'Hare and Z. Zhong, *Energy Environ. Sci.*, 2014, **7**, 3478-3518.
12. A. Al-Mamoori, A. A. Rownaghi and F. Rezaei, *Acs Sustainable Chem. Eng.*, 2018, **6**, 13551-13561.
13. B. Yuan, Y. Zhang, W. Du, M. Wang and F. Qian, *Appl. Energy*, 2019, **254**, 113583.
14. H. Sun, C. Wu, B. Shen, X. Zhang, Y. Zhang and J. Huang, *Materials Today Sustainability*, 2018, **1-2**, 1-27.
15. P. Melo Bravo and D. P. Debecker, *Waste Dispos. Sustain. Energy*, 2019, **1**, 53-65.
16. M. S. Duyar, M. A. A. Treviño and R. J. Farrauto, *Appl. Catal., B*, 2015, **168-169**, 370-376.
17. M. A. Arellano-Treviño, N. Kanani, C. W. Jeong-Potter and R. J. Farrauto, *Chem. Eng. J.*, 2019, **375**, 370-376.
18. L. Hu and A. Urakawa, *J. CO₂ Util.*, 2018, **25**, 323-329.
19. A. Bermejo-López, B. Pereda-Ayo, J. A. González-Marcos and J. R. González-Velasco, *J. CO₂ Util.*, 2019, **34**, 576-587.
20. M. Liu, L. Liang, X. Li, X. Gao and J. Sun, *Green Chem.*, 2016, **18**, 2851-2863.
21. J. L. Míguez, J. Porteiro, R. Pérez-Orozco, D. Patiño and S. Rodríguez, *Appl. Energy*, 2018, **211**, 1282-1296.
22. N. H. Florin and A. T. Harris, *Chem. Eng. Sci.*, 2009, **64**, 187-191.
23. J. B. Chen, Z. Y. Cai, X. X. Chen, X. H. Zheng and Y. Zheng, *Mater. Lett.*, 2016, **168**, 214-217.
24. S. M. Kim, P. M. Abdala, M. Broda, D. Hosseini, C. Copéret and C. Müller, *ACS Catal.*, 2018, **8**, 2815-2823.
25. Y. C. Hu, W. Q. Liu, H. Q. Chen, Z. J. Zhou, W. Y. Wang, J. Sun, X. W. Yang, X. Li and M. H. Xu, *Fuel*, 2016, **181**, 199-206.
26. A. Armutlulu, M. A. Naeem, H. J. Liu, S. M. Kim, A. Kierzkowska, A. Fedorov and C. R. Muller, *Adv. Mater.*, 2017, **29**, 1702896.
27. C. Chi, Y. Li, W. Zhang and Z. Wang, *Appl. Energy*, 2019, **251**, 113382.
28. M. Broda and C. R. Müller, *Fuel*, 2014, **127**, 94-100.
29. C. T. Yu, W. C. Chen, Y. P. Chyou and S. Y. Chen, *Energy Procedia*, 2013, **37**, 1246-1253.
30. H. Sun, C. M. A. Parlett, M. A. Isaacs, X. Liu, G. Adwek, J. Wang, B. Shen, J. Huang and C. Wu, *Fuel*, 2019, **235**, 1070-1076.
31. L. Y. Li, D. L. King, Z. M. Nie and C. Howard, *Ind. Eng. Chem. Res.*, 2009, **48**, 10604-10613.
32. A. Al-Mamoori, H. Thakkar, X. Li, A. A. Rownaghi and F. Rezaei, *Ind. Eng. Chem. Res.*, 2017, **56**, 8292-8300.
33. J. Phromprasit, J. Powell and S. Assabumrungrat, *Chem. Eng. J.*, 2016, **284**, 1212-1223.
34. A. Al-Mamoori, S. Lawson, A. A. Rownaghi and F. Rezaei, *Energy Fuels*, 2019, **33**, 1404-1413.
35. F. Gao, J. L. Huang, H. M. Sun, J. Hu, M. H. Wang, J. W. Mi and C. F. Wu, *J. Energy Inst.*, 2019, **92**, 1591-1598.
36. H. Sun, J. Wang, J. Zhao, B. Shen, J. Shi, J. Huang and C. Wu, *Appl. Catal., B*, 2019, **244**, 63-75.
37. X. Su, X. Yang, B. Zhao and Y. Huang, *J. Energy Chem.*, 2017, **26**, 854-867.
38. M. Keller and J. Otomo, *J. CO₂ Util.*, 2020, **40**, 101191.
39. E. Rezaei and S. Dzuryk, *Chem. Eng. Res. Des.*, 2019, **144**, 354-369.
40. F. Jiao, J. Li, X. Pan, J. Xiao, H. Li, H. Ma, M. Wei, Y. Pan, Z. Zhou and M. Li, *Science*, 2016, **351**, 1065-1068.
41. L. Zhong, F. Yu, Y. An, Y. Zhao, Y. Sun, Z. Li, T. Lin, Y. Lin, X. Qi, Y. Dai, L. Gu, J. Hu, S. Jin, Q. Shen and H. Wang, *Nature*, 2016, **538**, 84-87.
42. W. Zhou, K. Cheng, J. Kang, C. Zhou, V. Subramanian, Q. Zhang and Y. Wang, *Chem. Soc. Rev.*, 2019, **48**, 3193-3228.
43. X. B.Q., S. K.Q., Z. Q.M. and S. W.M.H., *Catal. Today*, 2000, 453-460.
44. S. Kattel, P. Liu and J. G. Chen, *J. Am. Chem. Soc.*, 2017, **139**, 9739-9754.
45. D. H. Kim, S. W. Han, H. S. Yoon and Y. D. Kim, *J. Ind. Eng. Chem.*, 2015, **23**, 67-71.
46. A. Ranjbar, A. Irankhah and S. F. Aghamiri, *J. Environ. Chem. Eng.*, 2018, **6**, 4945-4952.
47. E. T. Santos, C. Alfonsín, A. J. S. Chambel, A. Fernandes, A. P. Soares Dias, C. I. C. Pinheiro and M. F. Ribeiro, *Fuel*, 2012, **94**, 624-628.
48. Z. Kesic, I. Lukic, M. Zdujic, C. Jovalekic, V. Veljkovic and D. Skala, *Fuel Process. Technol.*, 2016, **143**, 162-168.
49. D. Hosseini, F. Donat, P. M. Abdala, S. M. Kim, A. M. Kierzkowska and C. R. Müller, *ACS Appl. Mater. Interfaces*, 2019, **11**, 18276-18284.
50. Y. Shen, Z. Cao and Z. Xiao, *Catalysts*, 2019, **9**, 423.
51. X. Jin, Y. Duan, D. Liu, X. Feng, W. Li, Z. Zhang and Y. Zhang, *ACS Appl. Nano Mater.*, 2019, **2**, 5769-5778.
52. A. C. Alba-Rubio, J. Santamaría-González, J. M. Mérida-Robles, R. Moreno-Tost, D. Martín-Alonso, A. Jiménez-López and P. Maireles-Torres, *Catal. Today*, 2010, **149**, 281-287.
53. C. Zou, Y. Kang, W. Wang, Y. Wang and R. Shi, *Energy Fuels*, 2019, **33**, 11830-11840.
54. D. Li, Y. Gong, Y. Zhang, C. Luo, W. Li, Q. Fu and C. Pan, *Sci Rep*, 2015, **5**, 12903.
55. H. Sun, J. Wang, X. Liu, B. Shen, Christopher M. A. Parlett, G. O. Adwek, E. John Anthony, P. T. Williams and C. Wu, *J. Mater. Chem. A*, 2019, **7**, 9977-9987.
56. H. Guo, X. Kou, Y. Zhao, S. Wang, Q. Sun and X. Ma, *Chem. Eng. J.*, 2018, **334**, 237-246.
57. M. Wenzel, L. Rihko-Struckmann and K. Sundmacher, *Chem. Eng. J.*, 2018, **336**, 278-296.
58. R. Liang, L. Shen, F. Jing, W. Wu, N. Qin, R. Lin and L. Wu, *Appl. Catal., B*, 2015, **162**, 245-251.
59. A. Hankin, J. Alexander and G. Kelsall, *Phys. Chem. Chem. Phys.*, 2014, **16**, 16176-16186.
60. P. Yu, J. Zhang, T. Zheng and T. Wang, *Colloids Surf. Physicochem. Eng. Aspects*, 2016, **494**, 241-247.
61. Q. Bi, X. Wang, F. Gu, X. Du, H. Bao, G. Yin, J. Liu and F. Huang, *ChemSusChem*, 2017, **10**, 3044-3048.
62. J. Deng, P. Ren, D. Deng and X. Bao, *Angew. Chem. Int. Ed.*, 2015, **54**, 2100-2104.
63. Q. Lu and F. Jiao, *Nano Energy*, 2016, **29**, 439-456.
64. J. Baltrusaitis and W. L. Luyben, *ACS Sustainable Chem. Eng.*, 2015, **3**, 2100-2111.
65. D.-Y. Lee and A. Elgowainy, *Int. J. Greenh. Gas Control*, 2018, **43**, 20143-20160.
66. E. De Lena, M. Spinelli, M. Gatti, R. Scaccabarozzi, S. Campanari, S. Consonni, G. Cinti and M. C. Romano, *Int. J. Greenh. Gas Control*, 2019, **82**, 244-260.
67. X. Luo, M. Wang, E. Oko and C. Okezie, *Appl. Energy*, 2014, **132**, 610-620.
68. S. Luo, L. Zeng, D. Xu, M. Kathe, E. Chung, N. Deshpande, L. Qin, A. Majumder, T.-L. Hsieh, A. Tong, Z. Sun and L.-S. Fan, *Energy Environ. Sci.*, 2014, **7**, 4104-4117.